India-Asia slowing convergence rate controls on the Cenozoic Himalaya-Tibetan tectonics

Ben S. Knight[1,2], Fabio A. Capitanio[2], Roberto F. Weinberg[2], Luca Dal Zilio[3]

[1]School of Earth and Planetary Sciences, Curtin University, Perth, 6102, Australia

[2]School of Earth, Atmosphere & Environment, Monash University, Clayton, 3800, Australia

[3] Seismology and Geodynamics, Institute of Geophysics, ETH Zurich, Zurich, Switzerland

ABSTRACT

The Cenozoic evolution of the Himalaya-Tibet Plateau, dictated by the India-Asia convergence, remains a subject of substantial ambiguity. Here, a thermo-mechanical model is used to show the critical controls of decelerating convergence on the formation and stabilization of distinctive tectonic structures during prolonged collision. At high constant convergence rates, similar to the late Paleogene India-Asia motions, the lower plate crust is injected beneath the overriding crust, uplifting a plateau, first, then is exhumed towards the orogeny front. Conversely, low constant convergence rates, similar to the Neogene India-Asia motions, induce crustal thickening and plateau formation without underplating or exhumation of incoming crust. Strikingly, models simulating the decelerating India-Asia convergence history portray a dynamic evolution, highlighting the transitory nature of features under decreasing convergence, as the orogen shifts to a new equilibrium. In the transitional phase, the slowing of convergence decreases basal shearing and compression, leading to extension and heating in the orogen interiors. This allows diapiric ascent of buried crust and plateau collapse, as accretion migrates to a frontal fold-and-thrust belt. The models provide insights into the multi-stage evolution of the long-lived Himalayan-Tibetan orogeny, from fast early growth of the Tibetan Plateau, through its transient destabilisation and late-stage internal extension, behind the expanding Himalayan belt.

Key words:
Himalayas, Geodynamics, Tectonics, Orogeny, Numerical modelling

1. INTRODUCTION

Since collision of India and Asia ~50 Ma, plate convergence has been accommodated by the structural evolution of the Himalayan mountains and the Tibetan Plateau (DeCelles et al., 2002; Guillot et al., 2003; Molnar and Tapponnier, 1975) (Figure 1a, b). However, how the convergence has been accommodated and its correlation with the structural evolution of the orogeny are pivotal unresolved questions, crucial for the interpretation of plate kinematics and orogenic processes.

The understanding of these processes is limited by uncertainties in three critical aspects: the India-Asia plate kinematics, the convergence motion partitioning, and the structuring of the orogeny. The India-Asia plate kinematics has been subject to debate, mostly related to the reconstruction and dating of the Indian Ocean floor (Liu et al., 2023; Molnar and Stock, 2009; van Hinsbergen et al., 2011). A robust feature of the convergence is the decreasing velocity throughout the Cenozoic (Figure 1c). This drops from values of ~18 to ~ 10 cm yr^{-1} before ~45 Ma, to between ~3 and ~5 cm yr^{-1}, possibly as low as ~2 cm yr^{-1} (Gibbons et al., 2015; Lee and Lawver, 1995; van Hinsbergen et al., 2011). Despite the evidence for deceleration, making clear connections between convergence and Himalaya-Tibetan Plateau orogeny evolution has been difficult, and attempts to relate convergence to Asian tectonics and Tibetan evolution have not provided clear answers (Clark and Royden, 2000; Molnar and Stock, 2009; Replumaz et al., 2004; Royden, 1997).

Ongoing uncertainty about the mechanisms accommodating convergence — whether it is through subduction, underplating, or indentation — has prevented firm assessments of mass balance. Crustal shortening estimates in the fold-and-thrust belt varies largely, from ~650 to 1000 km (DeCelles et al., 2002, 2001), even surpassing 1300 km (van Hinsbergen et al., 2011). These figures contrast with estimates derived from plate kinematics of total convergence ranging from 2000 to 3600 km since 50 Ma (Molnar and Stock, 2009; van Hinsbergen et al., 2011). The discrepancies may relate to assumptions regarding the subduction history of the Indian lithosphere (e.g., Jagoutz et al., 2011) or variations in the extent and nature of the Greater Indian margin (e.g., Liu et al., 2023).

Constraints from the deep Himalaya and Tibetan Plateau structures remain limited due to poor accessibility and resolution. Geophysical imaging does not clearly resolve the nature of the crust in the suture zone, and whether the Indian crust is accommodated in the beneath the orogeny, or up to ~30% is lost to subduction (Ingalls et al., 2016; Replumaz et al., 2010; Yakovlev and Clark, 2014), remains debated, preventing quantitative reconstructions of the orogeny (DeCelles et al., 2001). While a minimum subduction rate of the Indian lithosphere is ~2 cm yr^{-1} (Ader et al., 2012), likely consistent throughout the Cenozoic (Guillot et al., 2003) (Figure 1c, black), the diversity of convergence histories allows different hypotheses on crustal accommodation. This is due to open questions related to the time of collision and crustal thickening (Rowley, 1996), to the assessment of indentation, to uncertainties in crustal thicknesses prior to collision (Yin and Harrison, 2000), as well as the amount crust flowed or thrusted towards the Asian interior (Clark and Royden, 2000; Replumaz et al., 2004; Yakovlev and Clark, 2014).

The relationship between convergence, subduction, and structural style of the orogeny is grounded on the temperature- and strain rate-dependence of the strength of rocks. Extensive modelling reveals that during convergence, the advection of cold crust along with subducting lithosphere governs the temperature distribution within the orogeny, simultaneously dictating the basal shear rates between lithospheric plates (e.g. Faccenda et al., 2009; Knight et al., 2021; Piccolo et al., 2017; Vogt et al., 2017). These studies outline the influence of convergence rates on the structural make-up and tectonic style of orogens, offering a backdrop to explore more realistic convergence histories.

Here, the role of decreasing convergence rate on the evolution of collisional structures is tested. This has previously been employed to address the fate of the Indo-Asian lithosphere (Kelly et al., 2019; Liu et al., 2023), whereas we focus on the crust and its impact on the structural evolution of the orogeny. A two-dimensional computational model of subduction and collision at constant convergence rates is used, showing that structures remain active throughout convergence. In contrast, deceleration results in remarkably different and evolving structures where early-formed structures are destabilised or abandoned and the orogen reorganises.

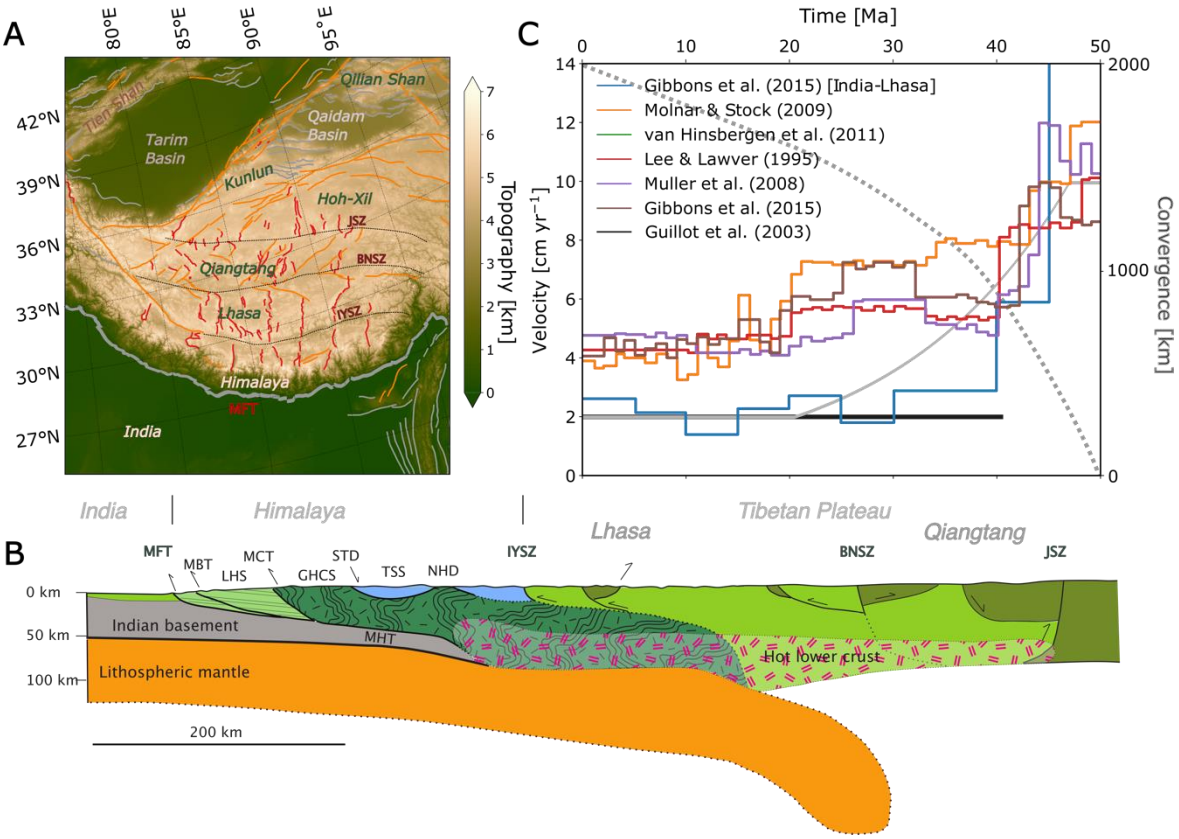

Figure 1: (A) Topography and major faulting of the Himalaya-Tibetan Plateau. Normal faults in red, strike-slip faults in yellow, IYSZ Indus-Yarlung-Tsangpo Suture Zone, BNSZ Bangong-Nujiang Suture Zone, JSZ Jinsha Suture Zone, MFT Main Frontal Thrust, MHT Main Himalayan Thrust, MBT Main Boundary Thrust, STD South Tibetan Detachment, LHS Lesser Himalaya Units, GHCS Greater Himalayan Crystalline Sequence, TSS Tethyan Sedimentary Units, NHD North Himalaya Domes. (B) Idealised cross section of the Himalaya-Tibetan Plateau, modified after Grujic et al., (2011); Searle, (2015) and Tapponnier et al., (2001). (C) Convergence velocities and subduction velocity (black) from Gibbons et al., (2015), Lee and Lawver, (1995), Molnar and Stock, (2009); Müller et al., (2008) and van Hinsbergen et al., (2011). Grey solid line is averaged convergence velocity used here, dashed line is total convergence.

2. Modelling convergence and collisional orogeny

In order to model the evolution of orogenic belts, a numerical approach is used that comprise the balance of forces due to subduction, buoyancy and internal stresses due to viscous and plastic deformation, the thermal balance between radiogenic heat, heat advection and diffusion during convergence, as well as the mass transfer due to erosion, transport and sedimentation (e.g., Gerya et al., 2008; Kelly et al.,

2019; Vogt et al., 2017) using an Eulerian finite element method with Lagrangian particles to solve for the viscoplastic flow of rocks (Beucher et al., 2019; Mansour et al., 2020).

The modelling of convergence aligns with established modelling procedures (Knight et al., 2021; Vogt et al., 2017). Convergence of two continental plates is utilised from the time of collision, separated by a predetermined weak zone, favouring subduction (Figure 2a). During convergence, the crust decouples from the subducting mantle lithosphere causing crustal shortening and thickening, i.e., orogeny. Convergence is modelled by imposing a horizontal velocity across the crust and lithosphere, as outlined in Knight et al. (2021). Constant velocity models of 10 and 2 cm yr^{-1}, bracketing the inferred India-Asia motions, are compared with a model where the convergence rate varies between these values (Figure 1c, grey solid line). All models run until a minimum convergence of 2000 km is accommodated, comparable to the India-Asia Cenozoic convergence and the reconstructed continental margin (Guillot et al., 2003; Liu et al., 2023). The full model setup is described in Appendix A.

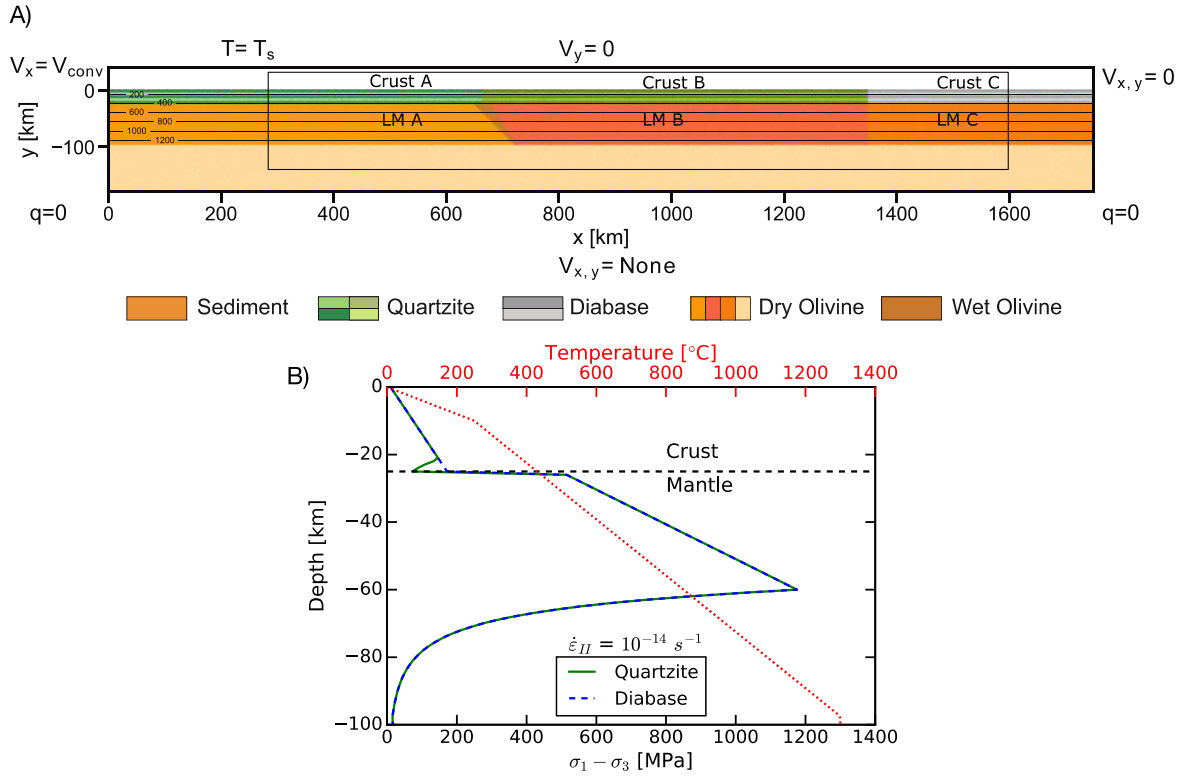

Figure 2: A) Model setup. The convergence velocity is applied to the left boundary of the lithosphere and crust, with inflow and outflow across the sticky air layer. The top

boundary is free slip, the right boundary no slip and the bottom boundary is unconstrained. The left, top and right boundaries have zero heat flux, whilst the temperature of the bottom boundary is unconstrained. The black box marks the area show in subsequent figures. LM = lithospheric mantle. B) Strength and temperature profile displaying the difference in strength between crust A/B (quartzite) and C (diabase) above 25 km depth, with both containing a dry olivine lithospheric mantle below, at constant strain rate of 10^{-14} s^{-1}.

3. Convergence history controls on orogeny structures

3.1 Fast convergence model

In the fast convergence model 2000 km of convergence is achieved at a constant rate 10 cm yr^{-1} over 20 Myr. The crust of both plates folds to form a proto-wedge, in the initial stage of the collision (Figure 3, 4 Myr), and is then thrusted over the incoming crust (dashed line), by ~8 Myr. The downgoing crust reaches depths of ~50 to 60 km and pressures of 1.6-2 GPa (Figure 4a, red), then decouples from the subducting lithospheric mantle and injects along the upper plate's lithosphere-crust contact (Figure 3, 8 – 12 Myr), uplifting the overriding crust into a plateau. The deformation is driven by the basal shearing, which weakens the crust and forces flow as it thickens and heats up. Part of this crust remains buried at 1.5-2.0 GPa/~600 ˚C (Figure 3 and 4 red symbols) until the end of the model run.

Once ~600 km of convergence is accommodated, the downgoing crust reaches deeper, ~100 km, and then exhumed towards the orogeny front (Figure 3, 16 Myr, dotted line). The uplifted plateau act as a rigid buttress, counterbalancing the channel flow pressure and forcing the resurfacing of incoming crust to the front of the orogeny through a return (counter) flow, at velocities of similar magnitude to the convergence rate. The expanding exhumation channel gradually removes most of the proto-wedge units (Figure 3, 20 Myr). The rocks within these units undergo multiple burial and exhumation episodes, from ultra-high pressure to high temperature, and subsequently back to medium pressure conditions, exemplifying the "yo-yo tectonics" (Figure 3 12-20 Myr, and Figure 4a, yellow symbols).

By the end of the modelled time, the plateau's crust reaches a thickness of ~70 km, where extant folded crust is stacked above the exotic crust, injected in the early (Figure 3, 20 Myr, red diamond) and late stages (blue diamond). Minor

translation of the orogeny over the upper plate interior occurs over along a steep

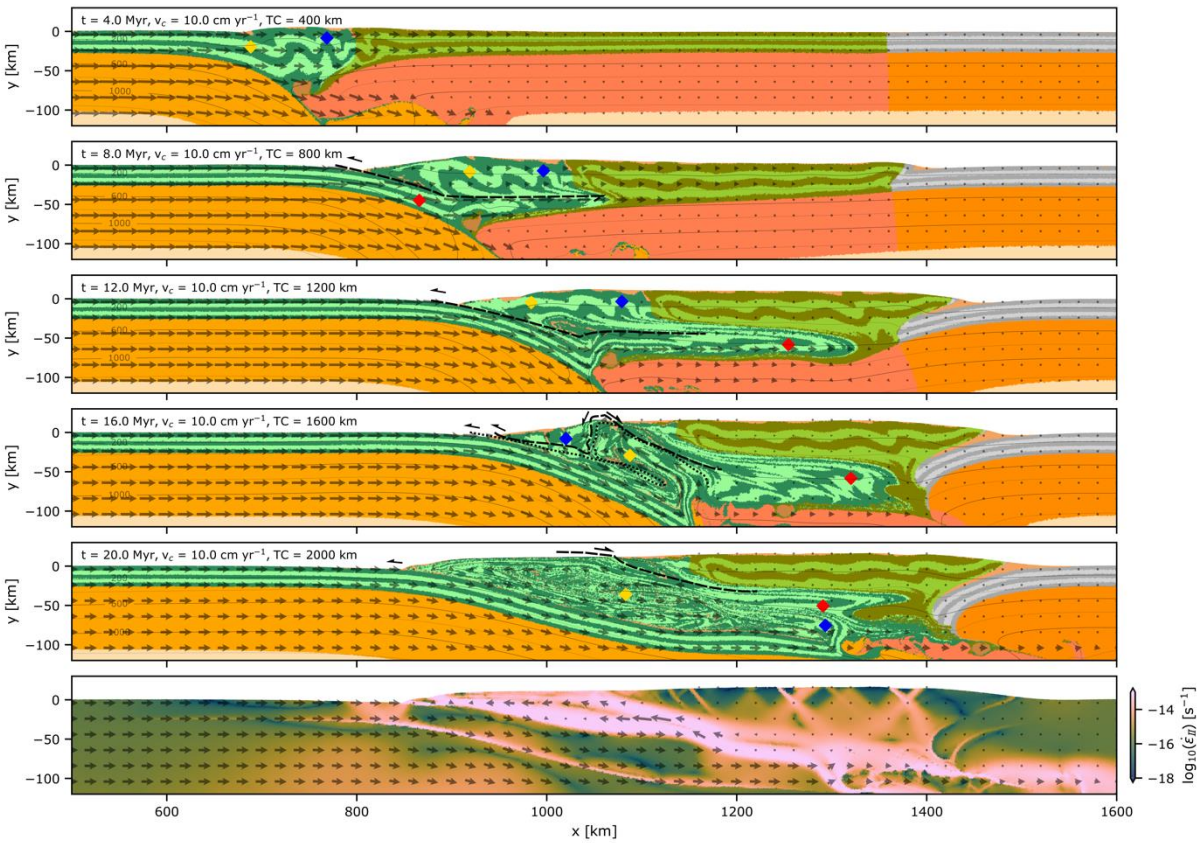

inward-dipping thrust.

Figure 3: Fast and constant convergence velocity model v_x = 10 cm yr^{-1}. Blue, red and yellow symbols indicate locations of PTt paths in Figure 4. t is time, v_c is convergence velocity and TC is total convergence.

The topography at the end of the run shows a plateau at ~7 km high and ~700 km wide (Figure 4d, blue dashed line), sloping towards the foreland, where no thrust-and-fold belt forms at the orogens front. Due to the short duration of the model, erosion and sedimentation are negligible. As the fast convergence persist, isotherms are drawn to shallow depths in the exhumation channel, bordered by a cooler plateau interior. This is reflected by the final heat flow (Figure 4e, blue dashed line) with values of ~160-200 mW m^{-2}, in the exhumation channel, bordered by regions with heat flow of 40-50 mW m^{-2}.

The late stage of this model shows the deep underthrusting of the extant crust of ~170 km past the suture zone (Figure 3, 20 Myr). The downgoing lithosphere underthrusting replaces the upper plate's lithospheric mantle, as it delaminates (LMB

in Figure 2, dark orange), and is accompanied by a dip decreases and a mild widening of the orogeny. Convergence is persistently accommodated by the crustal return flow (Figure 3, bottom panel), shown by the PT paths of the proto-wedge units (Figure 4a, blue and yellow diamonds), entrained deeply beneath the plateau reaching UHP conditions, that is >2.5 GPa/800 ˚C. while the plateau interior experiences minimal deformation and no frontal fold-and-thrust forms.

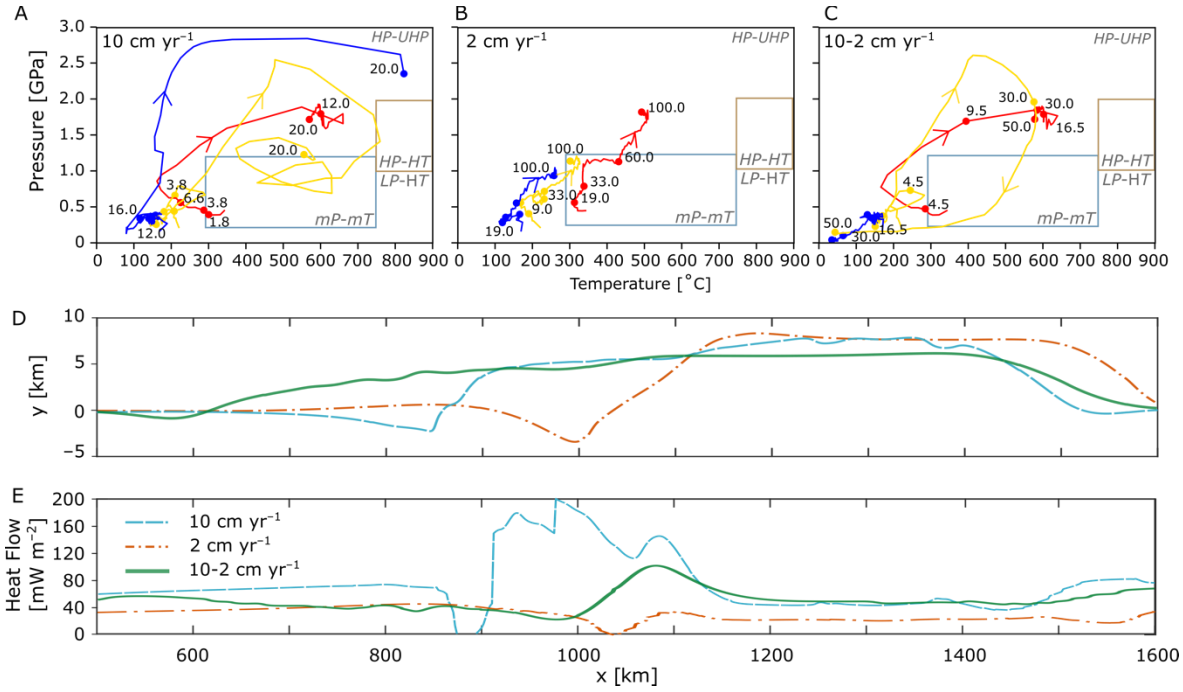

Figure 4: Modelled PTt paths, topography and heat flow. (A) v_x = 10 cm yr^{-1}, (B) v_x = 2 cm yr^{-1}, and (C) v_x = 10 to 2 cm yr^{-1}. Notice for 10 cm yr^{-1} in (A), all trackers reach high pressure (HP) conditions, and the yellow tracker undergoes several cycles of burial and exhumation within the forced convection at the orogenic front. Location of trackers shown in Figure 3, 5 and 6. (D) Topography and (E) heat flow of the models at the end of the model, after 2000 km convergence.

3.2 Slow convergence model

In the model with a slow constant convergence rate of 2 cm yr^{-1} over 100 Myr to reach 2000 km of convergence, a distinct structural style emerges, with predominant pure-shear thickening, with folding and minor faulting, forming a flat plateau with sloping flanks analogous to the fast model, despite the different internal structures.

Spanning most of the modelled duration, until approximately 80 Myr — translating to around 1600 km of convergence — the slow convergence is accommodated by crustal folding, sequentially accommodated into the upper plate, culminating in a cohesive crustal plateau, with a uniform thickness of around 70-80 km (Figure 5, 20 to 80 Myr). In contrast to the fast convergence model where the short duration minimises diffusion, at slow convergence rates, thermal diffusion re-equilibrates efficiently the perturbed geotherms, leading to a thicker colder crust forming a fold belt, while no channel flow occurs (Figure 5, 80 Myr). The *PTt* paths (Figure 4b) show that all units (marked by red, blue, and yellow symbols) follow an average gradient of ~5-10 ˚C km^{-1}, maintaining a temperature ceiling of ~500 ˚C at ~2 GPa (red), showing that the orogeny is cooler by ~100 ˚C than the fast model at analogous pressures.

In the late stages, ~80 to 100 Myr (Figure 5, 100 Myr), the incoming crust is buried deeply accommodated at the base of the orogen. The thickened crust load favours thrusting bordering the orogeny and shearing of incoming crust at the base of the plateau. These are illustrated by the strain rates and velocity fields (Figure 5, bottom panel) showing localisation along the outer thrusts and distributed deep crustal strain beneath the plateau. Another important difference is that no exhumation occurs at the front of the orogen and crustal flow is a late-stage and minor feature. In contrast to the fast model, the two crusts remain separated by a steep suture zone.

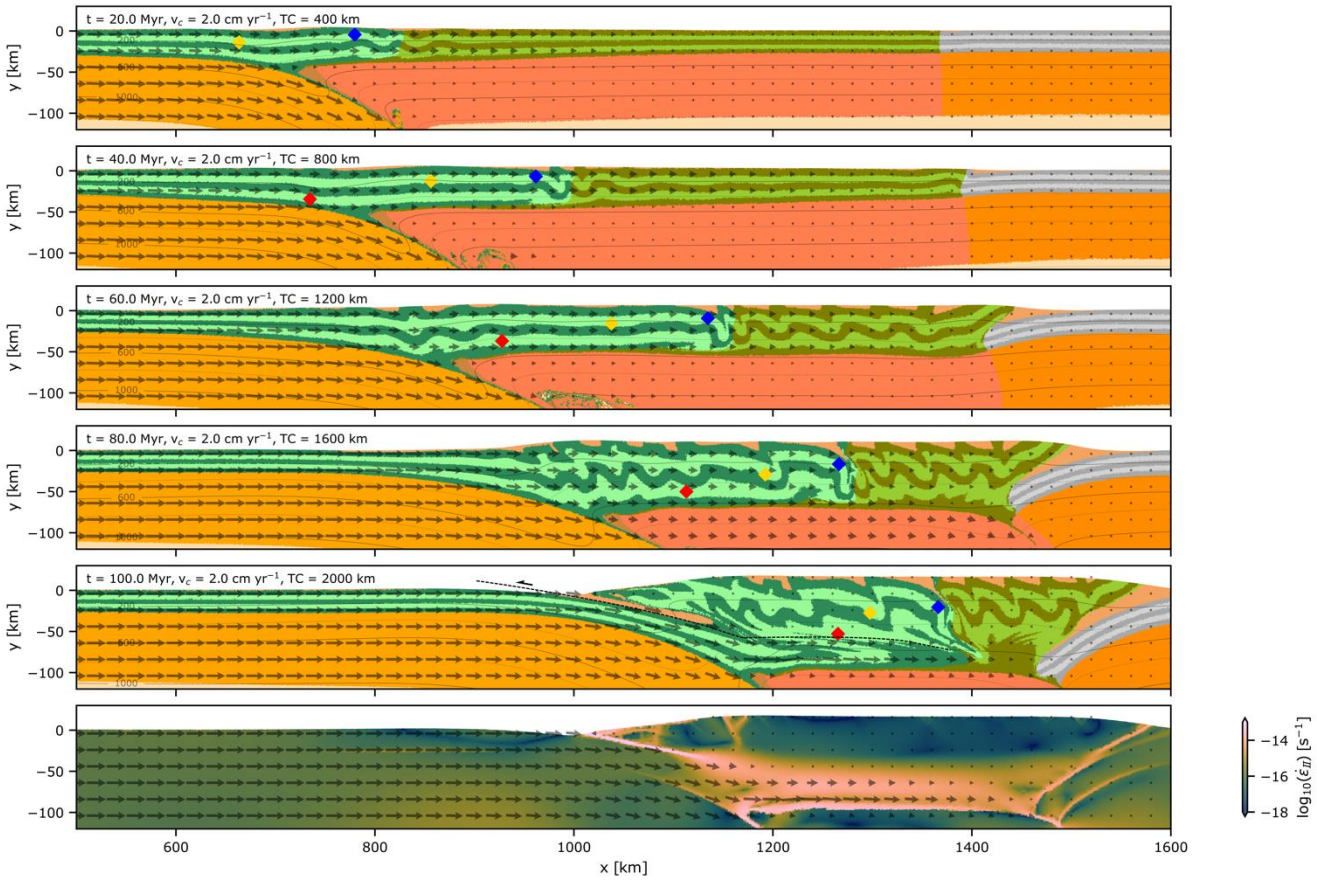

Figure 5: Slow and constant convergence velocity model, vx = 2 cm yr–1. Blue, red and yellow symbols indicate locations of PTt paths in Figure 4. t is time, vc is convergence velocity and TC is total convergence.

The orogen in this model develops a plateau, ~600 km wide and of similar elevation to the plateau in the fast model, ~7 km (Figure 4d, red dash-dotted line), although developing remarkably different structures. The slow convergence favours diffusion that results in low heat flow, < ~40 mW m^{-2}, with the lowest values in the plateau (Figure 4e, red dash-dotted line). Erosion and sedimentation are intensified due to the model duration, although limited by the gentle slopes, with thicker sediment layers on the plateau and entrained in the orogen by thrusting, while crustal structures on the upper plate buttress are similar to that of the previous model.

Lower convergence velocity coupled with reduced orogeny temperatures, precludes the deformation of the downgoing lithosphere, which is preserved the beneath the orogeny (Figure 5, 100 Myr) and less deformed than the fast convergence model. A fundamental difference is the nature of the orogenic front and

the bulk of the crustal plateau overlaying a layer of incoming crust in the fast convergence model, while in the low convergence the two crusts are side-by-side, separated by a steep suture.

3.3 Decelerating convergence model

The model with decelerating convergence reproduces structures similar to the fast convergence model in the early stages, which change as the convergence rates decrease. As convergence and compression decrease, the perturbed thermal gradients in the orogen progressively re-equilibrate, altering the rheology of the later

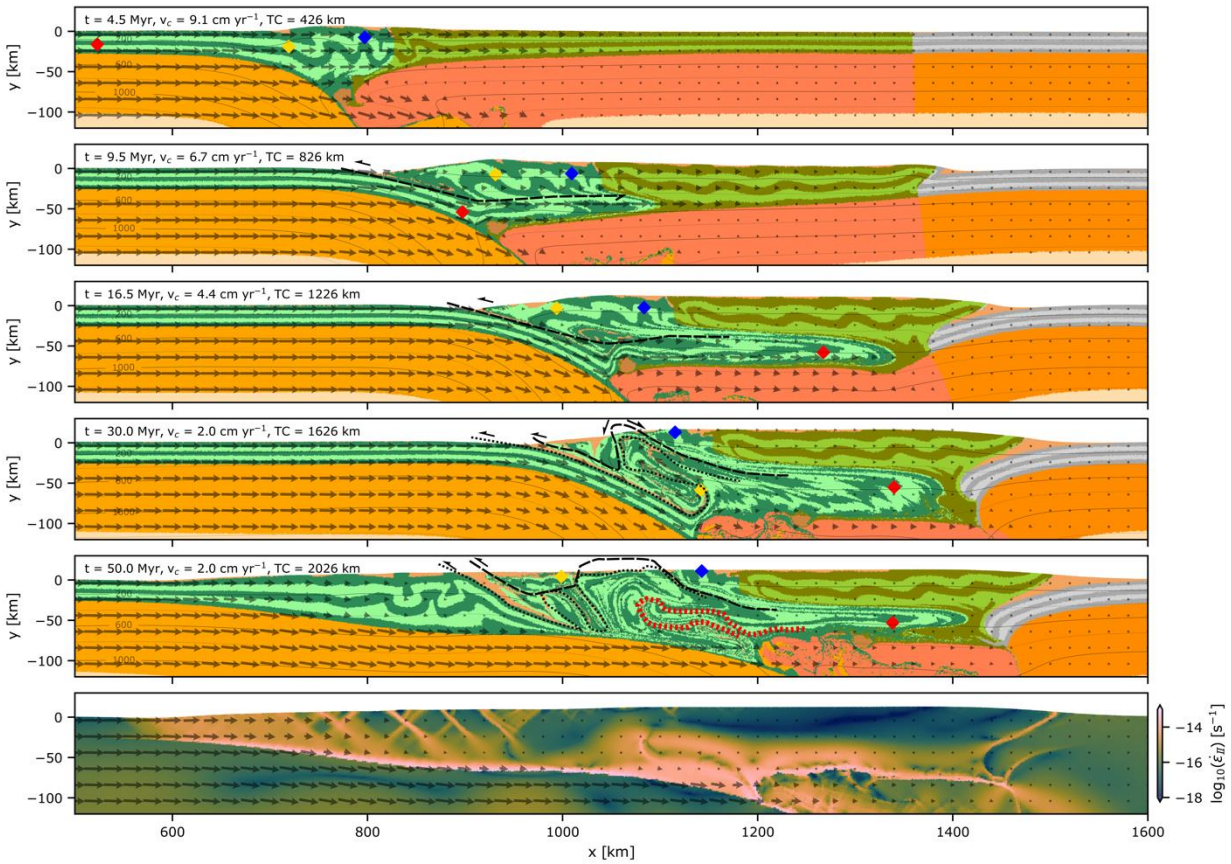

stage, resulting in a significantly different orogen.

Figure 5: Decreasing convergence velocity model. Velocity varies from v_x = 10 to 2 cm yr^{-1} (see Figure 1c). Blue, red and yellow symbols indicate locations of PTt paths in Figure 4. t is time, v_c is convergence velocity and TC is total convergence.

In the initial stage, deformation of the extant crust is comparable to that in the fast-convergence model, with folding and thrusting of an initial proto-wedge, followed by injection of incoming crust into the extant plate, ~200 km along the crust-

lithospheric mantle contact (Figure 6, 16.5 Myr, red symbol). Subsequently, as in the fast convergence model, the incoming crust is buried deeper, to ~100 km (Figure 6, 30 Myr), then exhumed by return flow, and no longer injected beneath the plateau. In this state, the return flow forms part of the proto-wedge (Figure 4c, yellow symbols), and *PT* paths show the same cycle of burial to UHP conditions (~2.0 GPa) and exhumation to shallow depths (Figure 4c, yellow symbols).

In the remainder of the model the decelerating convergence induces a unique structural reorganisation and outward deformation migration. In this stage, ~400 km of convergence is accommodated between 30 and 50 Myr. The incoming crust, no longer buried deeply, decouples from the lithospheric mantle at ~ 50 km depth, accruing in the front of the orogen, forming a broadening frontal fold-and-thrust (FAT) belt. In this case, the fold-and-thrust belt grows outwards, as opposed to the slow convergence model, where the shortening and thickening occurs in the orogen interior. By the end of the model, the width of the orogen has expanded to ~1000 km (Figure 6, 50 Myr).

Another unique feature of this model is the relaxation during late stages of both horizontal compression and strong temperature gradients, with heating of the deeply buried cold crust, emplaced during the fast convergence stage. While the channel flow ceases by ~16.5 Myr, the heating and progressive extension in the later stage, drives the diapiric ascent of newly weakened deep crust into the exhumed crust above (Figure 6, 50 Myr, red dotted line). The crustal doming is passive, as the flow in the exhumation channel has ceased, indicated by the vanishing of velocity vectors in Figure 6, 50 Myr (x = 1000 to 1200 km) and strain rates (bottom panel) in the previously active basal flow. Higher deformation rates in the ascending diapir and neighbouring channel flow illustrate the activity of these structures, as well as the active faulting and folding at the front and back of the orogen, as in the slow constant convergence model. The PTt path of the entrained units (yellow) shows initial cold *P/T* gradients followed by entrainment to *UHP* conditions, reaching temperatures of ~600 ˚C, then returning to the surface (Figure 4c).

The final topography in this model has similar features to the previous models, with a flat plateau and a sloping orogenic front and rear structures (Figure 4d). Compared to the fast and slow models, the topography is ~1 to 2 km lower and ~300

km wider. The heat flow also shows higher values on the exhumed crust, typical of the fast convergence models, although reduced to <120 mW m^{-2}, lower values in the plateau, ~60 mW m^{-2}, and 40 to 60 mW m^{-2}, in the frontal FAT belt (Figure 4d). The decelerating convergence rate accentuates erosion and sedimentation, allowing thicker sediment layers in the outer domains of the orogen. The structures of the upper plate, where the orogen overthrusts the overriding lithosphere, remain consistent with other models, with active thrusting. In this model, the plateau's lithospheric mantle is partially removed, that is, between the almost complete delamination and minor thickening of the fast and slow convergence models, respectively.

4. DISCUSSION

4.1 Reconciling the Himalaya-Tibetan Plateau structuring with plate convergence

Comparison of models with the Himalaya-Tibetan Plateau provides insights into the joint evolution of the collisional margin and plate motions, substantiating the discussion of the present-day deformation in the area.

In our assessment of the role of convergence rate, only the model with a decreasing convergence velocity mirrors first-order features of the India-Asia collisional margin. The Himalayan rocks belonging to India and the Asia rocks forming the Tibetan Plateau, TP (Figure 1) are divided by the Indus-Yarlung-Tsangpo suture (IYSZ), separating thickened crust to the north, from the Himalayan fold-and-thrust belt (H-FAT), which has comparable structures all along the chain front (DeCelles et al., 2002). The development of the H-FAT belt is well constrained, with active faulting younging to the south (DeCelles et al., 2001; Goscombe et al., 2018), now active along the Main Boundary Thrusts (MBT). The H-FAT extends ~400 km from the front to the IYSZ above the Indian plate, underlain by a single, continuous seismic reflector (Gao et al., 2016), which dips gently beneath the orogen and deepens further north along a step, reaching the IYSZ (DeCelles et al., 2002, 2001; Nelson et al., 1996; Zhao et al., 1993). The H-FAT is overthrusted along the Main Central Thrust (MCT) by the Greater Himalayan Crystalline Sequence (GHCS), where deep-seated crustal rocks have been exhumed in a channel (Beaumont et al., 2001; Grujic et al., 1996). These are overlain by the Tethyan Sedimentary Sequence

(TSS), along the South Tibetan Detachment (STD) (DeCelles et al., 2001), which remained structurally high in the edifice since collision inception.

These features are reproduced by the model with decreasing convergence. The model reproduces the frontal FAT belt, structurally beneath a wedge of complexly deformed and exhumed deep crustal rocks, similar to the GHCS, topped by the proto-wedge units, akin to the TSS. Except for the TSS, the other features are not captured by constant convergence models, which either do not develop a FAT belt, when too fast, or do not develop exhumation of deep rocks, when too slow. The final width of the FAT in the model is ~400 km, in agreement with the width of the H-FAT, and reproduces the deep structure of the Indian lithosphere and orogen, with folding-and-thrusting above a step-like basal decollement reaching ~70 km depth beneath the suture zone, then plunging into the mantle (Zhao et al., 1993).

The TP extends far into the Asian plate, having widened with the evolution of the orogeny (Tapponnier et al., 2001). Immediately north of the IYSZ is the Lhasa Terrane (Figure 1a), ~500-700 km wide, supported by a ~60-80 km thick crust (Kumar et al., 2019). The Lhasa Terrane's is underplated by Indian crust, emplaced along the Moho between the Asian crust and lithosphere (DeCelles et al., 2002; Kumar et al., 2019; Streule et al., 2010), ~200-400 km further north than the IYSZ (Figure 1b). The models reproduce this geometry with injection of incoming crust below the Moho of the extant crust, ~200 km from the suture zone at the surface, uplifting a plateau with a similar crustal thickness and elevation to the TP, during the fast-converging stages.

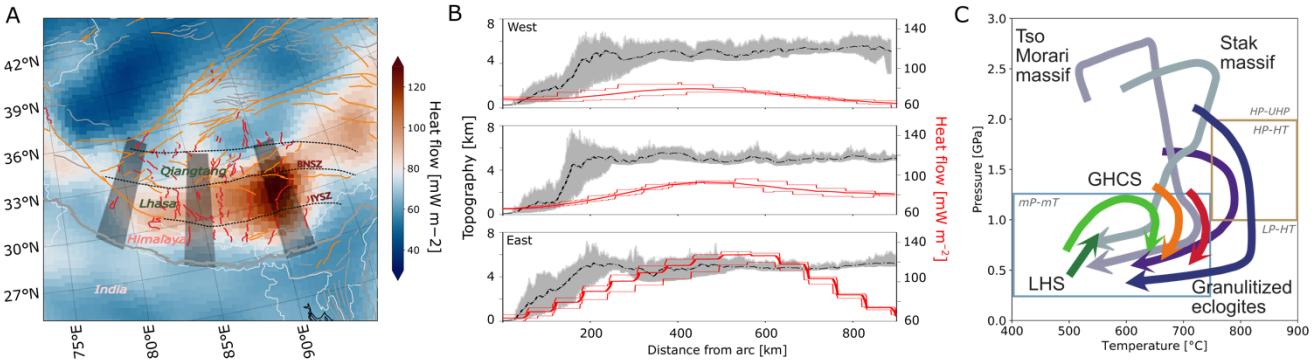

Figure 6: A) Heat flow map of the Himalayan-Tibetan region(Lucazeau, 2019). B) Min, max and average heat flow (Lucazeau, 2019) and topography (Robinson et al.,

2014) profiles from the West, centre and Eastern regions (grey boxes in A). C) Idealised P-T-t paths from the Himalayas, showing variations depending on location within the orogen (Kohn, 2014).

The results show that the models' topography comparison to the present-day orogen might not be diagnostic, instead the heat flow provides better constraints. A plot of three sections of the India-Asia collisional margin shows an overall flat topography (Figure 7), with consistent average elevation of ~5000 m ± 1000 m, sloping towards the Himalayan front. The plateau can be fit similarly by the different models proposed, all reproducing a flat top and sloping flanks (Figure 4d). The heat flow in the models show that faster convergence maximises heat flow in the exhuming frontal portion, whereas slower convergence minimises heat flow perturbations (Figure 4e). The distribution of heat flow along the orogeny is essentially symmetrical, with values increasing from ~40 mW m^{-2} in the foreland, to a maximum of 80 to 130 mW m^{-2}, then decreasing to ~60-80 mW m^{-2} towards the northern Tibet (Figure 7a, b). These values are comparable to the decelerating model's heat flow, with 40-60 mW m^{-2} in the foreland increasing to ~110 mW m^{-2}, then reaching ~60 mW m^{-2} in the plateau (Figure 6e). Additionally, the observed location of the heat flow peak in the elevated orogeny interior (Figure 7b) is reproduced only by the decreasing convergence model presented.

Additional support for the role of the convergence rate is provided by a comparison between models and evolution of the India-Asia collisional orogeny (Figure 8). The orogeny began with the folding of the Tethyan Sedimentary Sequence around 50 Ma (Figure 8a, TSS), which remained on top of the Himalayan sequence (Streule et al., 2010). The change of lower crust to eclogite (Pichon et al., 1992; Spain and Hirn, 1997) supported by (ultra-)high-pressure eclogite facies (Figure 7c) found in the Kaghan area, north Pakistan, and the Tso Morari complex, NW India, suggest the Indian crust reached depths of >50 km between 47 and 43 Ma (de Sigoyer et al., 2000) (Figure 8a, green star) before being exhumed.

The folding of the upper crust in the models matches the initial folding in the Tethyan Sequence (Figure 5) as well as the burial of cold incoming crust to depths >50 km by ~43 Ma (Figure 5), and exhumation after 34 Ma. Even though tracking the PTt in the models might not exactly match the observed, the modelled paths are

comparable to those for the Tso Morari units, reaching P> 2 GPa and then warming during decompression to ~600 ˚C (Figure 7c).

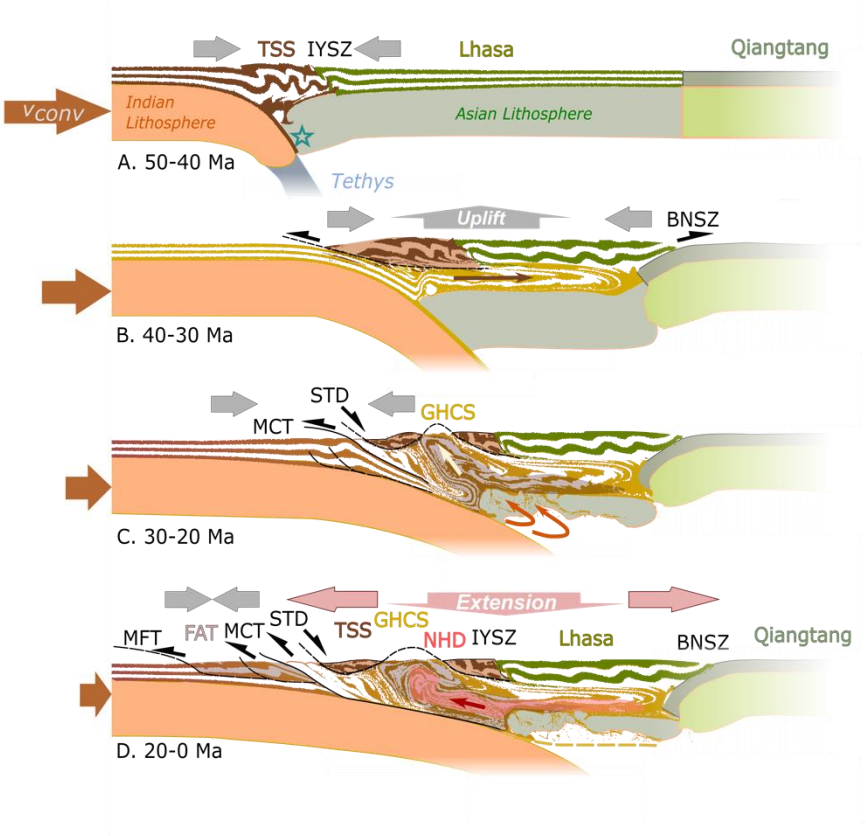

Figure 7: Sketch of the evolution of the Himalaya- Tibetan Plateau. Partially modified from (Streule et al., 2010). Black lines, major tectonic contacts, colored, major units, see Figure 1.

Between ~40 and ~30 Ma, part of the Indian crust emplaced beneath the Lhasa terrane crust (DeCelles et al., 2002; Streule et al., 2010) (Figure 8b). This played a part in the evolution of the Plateau, causing the crust to thicken and uplifting the TP with minor deformation (Figure 8b, brown arrow). Our models with fast and decreasing convergence show similar crustal flow from ~43 to 35 Ma (Figure 3, 5) in the decreasing convergence model.

The exhumation of deep-seated Indian crust in the Greater Himalayan Crystalline Sequence (GHCS) through ductile flow (Grujic et al., 1996) (Figure 8c, yellow arrow) is constrained by monazite U–Pb ages from ~38 Ma, although varies along the Himalaya (Finch et al., 2014; Godin et al., 2006; Goscombe et al., 2018; Searle, 2015; Searle and Hacker, 2019), lasting until the emplacement of the North

Himalayan Domes, between 21 and 12 Ma (Goscombe et al., 2018), possibly subsiding when the Himalayan FAT began to develop ~18 Ma (Gao et al., 2016; Searle, 2015) until the formation of the Lesser Himalaya units (Figure 8d, LH). Both the fast and decreasing convergence models exhibit burial and exhumation of the incoming crust (Figure 8c). The decreasing convergence model shows exhumation onset by ~34 Ma, active until ~8 Ma, with the earliest shallow emplacement of exhumed units at ~25 Ma (Figure 5, 6). These characteristics agree with long-lived metamorphism with cold *P-T* gradients culminating in high-grade peak metamorphic conditions by ~27-19 Ma (Goscombe et al., 2018) and along-orogen averaged metamorphic temperatures of 600-650 ˚C. Peak temperatures of 850 ˚C locally found in the GHCS (Goscombe et al., 2018), are reached only for the fast convergence models, likely due to an underestimate of the convergence rate prior to ~25 Ma in our slowing convergence model.

After ~25 Myr, exhumation of deeply buried GHCS units and the forward migration of strain in the Himalayan front record the transition between fast and slow convergence styles. Isothermal decompression followed by rapid cooling is registered throughout much of the GHCS. The timing of the rapid cooling phase varies but is typically <20 Ma (Searle, 2015). Shallow rock emplacement and cooling paths can only be reproduced by models with decreasing convergence, supporting the idea that exhumation is favoured by slowing convergence (Maiti and Mandal, 2021). The extrusion of deep crust resulted in the emplacement of the GHCS between the STD and the MCT (Godin et al., 2006), leading to inverted metamorphic isograds above the MCT, in a “hot-on-cold” sequence (Goscombe et al., 2018; Hunter et al., 2018; Searle, 2015) and right-way-up metamorphic isograds below the STD (Godin et al., 2006; Searle, 2015) (Figure 8c). This is reproduced in all the models at high convergence rate (Figure 3 and 6, dashed black line). The transition reflects the conditions proposed for the GHCS, with high convergence velocity required to bury rigid crust at the front of the orogen, followed by exhumation driven by released pressure gradients (Godin et al., 2006; Searle, 2015), here explained by lowered convergence rates. Our models suggest a complex evolution of these units, in agreement with inferred post-channel, post-exhumation modifications and the TSS as protolith for part of the GHCS (see Godin et al., 2006).

In the model's transitional stage, slowing convergence allows the thermal re-equilibration of the deeply buried cold crust beneath the plateau. The ensuing warming and weakening of the deep crust and formation of buoyant, low viscosity crustal diapirs, between ~30 Ma and ~8 Ma (Figure 8c, grey area). This mechanism is compatible with the late-stage deformation of the original channel beneath the Tibetan Plateau (Jessup et al., 2006), with the Miocene doming the North Himalayan Domes (NHD, Jessup et al., 2019). The NHD indicate are interpreted as evidence of extension concurrent with contraction ongoing elsewhere (Lee et al., 2000) (Figure 8d, grey arrow for contraction, pink arrows for extension). At depth, a low viscosity, partially molten, extending from the GHCS to the Lhasa Terrane (Nelson et al., 1996; Unsworth et al., 2005), is inferred from low seismic velocity (Figure 8d, red area). The ductile flow of this layer (Nelson et al., 1996) may explain the general thinning of the Lhasa Terrane's lithosphere highlighted (Figure 1b) and potassic volcanism between 30 and ~10 Ma (Wang et al., 2014). Thermal relaxation is a key feature of decreasing convergence models, switching from fast burial of cold crust to slow burial and heating due to thermal equilibration. Instead, models with a constant convergence rate attain a stationary equilibrium, which may be relaxed post-orogeny.

As convergence rates slow the orogeny reaches a new equilibrium. The India-Asia orogeny has widened through the onset of the Himalaya frontal fold-and-thrust belt above a shallow dipping lithosphere, by ~18 Ma (Figure 8d), then becoming the primary process accommodating convergence at 12 Ma (DeCelles et al., 2002, 2001). The coeval extension along the STD as the front contracted is a known feature of the late-stage Himalayan orogeny (Burchfiel et al., 1992), captured by our models. In the Himalayan front, convergence is currently accommodated along the Main Frontal Thrust (MFT), at rates of 2 cm yr^{-1} (Ader et al., 2012). The remainder of the convergence is likely accommodated through lateral extrusion towards east Asia and indentation (Liang et al., 2013). The FAT emerges only at slow convergence, however, at constant slow convergence the FAT remains in the orogeny interior, as it contracts, whereas for slowing convergence the FAT belt migrates to the orogen's front as the orogen interiors extends.

4.2 Speculations on the growing Himalaya and collapsing Tibetan Plateau

The stages of evolution illustrated, from the initial rapid build-up of a plateau achieved at fast convergence rates, through transition to a final stage of outward accretion and internal extension, provides a context for interpreting the Himalayan-Tibetan Plateau topography evolution and its current deformation state.

Paleoaltimetry, paleobotanical, magnetostratigraphy, sedimentology, paleocurrent measurements, $^{40}Ar/^{39}Ar$ dating and fission-track studies show that the elevation of the Lhasa, Eastern Tibet and northern Qiangtang Terranes increased from ~1000 m to ~4000 m between ~50 and ~35 Ma (Ding et al., 2022; Wang et al., 2014). Our slowing convergence model supports these estimates, showing that ~80% of the final model topography could have been achieved between 42 and 37 Ma due to crustal thickening (Figure 9a, blue line). A similar outcome is shown in the fast convergence model (Figure S1), suggesting early thickening is a consequence of fast convergence.

GPS, seismic and Quaternary strain show current Plateau extension (e.g., England and Molnar, 2005), behind the compressive Himalayan front, with localised (tectonic) topographic lowering in the Lhasa Terrane (Zhao et al., 2023). The lowering of topography is mostly explained by the extension due to the east-ward Plateau expansion (Clark and Royden, 2000), evidenced by widespread NS-trending rifts active from 19 Ma onwards (Mitsuishi et al., 2012; Wang et al., 2014). However, the STD and the granite-gneiss domes in the Tethyan Himalayas indicate a NS extension event that is older than, possibly contemporaneous, with the EW extension that formed the rifts (Mitsuishi et al., 2012). Additionally, the component analysis of current strain rate (Wang and Barbot, 2023) shows convergence-parallel extension localised in the Lhasa Terrane of comparable magnitude to the perpendicular extension, then part of the extension may be associated with the orogeny, as in our model.

Our slowing convergence model reproduces the increase in elevation until the plateau “collapse” at the same time of the widening and FAT formation (Figure 8a, blue line). The elevation reaches ~6.5 km, as in the constant velocity models, keeping a rather constant width (Figure 9a, magenta lines), equivalent to 50% of today’s plateau width as measured at heights of 3 and 1.5 km. However, with the forward migration of the deformation to form the frontal FAT after ~18 Ma (Figure 9a, brown line), the plateau widens and lowers, matching the width and altitude of the Tibetan plateau today (Figure 9a). This is in agreement with paleobotanical and

geological constraints on eastern Himalayan elevations, which rapidly reached >3000 m starting 20-18 Ma (Ding et al., 2022), and attained comparable values to present-day by ~12 Ma (Wang et al., 2014). The altitude drops in the model by ~1500 m between ~18 and ~8 Ma, is comparable to the inferred topographic lowering of ~1000 m (Wang et al., 2014) in the plateau. The model shows that this follows the heating and ascent of the deep crust in the channel zone and then as a dome, as the compression in the interior of the orogen vanishes. This is marked by an increase in the heat flow in the orogen front (Figure 8b, light green) and a minor increase in the inner plateau (dark green), as the FAT widens and convergence rates decrease below ~3 cm yr^{-1} (brown dashed line).

Models proposed for the Plateau collapse invoked the dissipation of excess potential energy, relating extension to variations of boundary conditions (Wang et al., 2014, and references therein). Here, the models have shown that indeed the slowing India-Asia convergence lowers the dynamic support of the elevated edifice, allowing release of potential energy, lowering altitudes as Tibet undergoes extension. This is facilitated by heating of the deep crust, while deformation migrates to a fold-and-thrust belt in the Himalayan front.

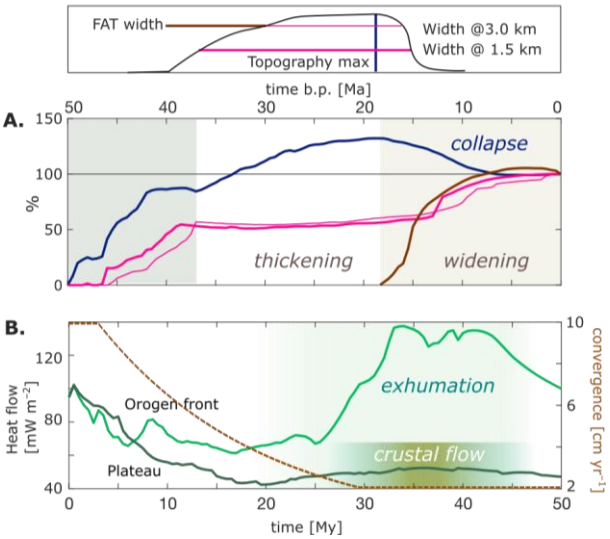

Figure 8: Evolution of (A) height (blue) of the orogeny, width measured at 3 and 1.5 km height of the wedge (magenta), and the fold-and-thrust belt (FAT, brown) with respect to the final stage. (B) Maximum heat flow in the orogen front (light green) and in the plateau domain (dark green), and convergence velocity (brown). Exhumation coincides with increased heat flow in the orogenic front.

4.3 Comparison with previous models

The formation of the Himalaya-Tibetan Plateau and its elevation have served as a paradigm for the understanding of collisional orogeneses (e.g., Ding et al., 2022). Different models have been proposed for the uplift of Tibet, such as the underthrusting of Indian lithosphere beneath the Plateau, injection of Indian crust beneath Tibetan crust, or distributed shortening and partial lateral extrusion (e.g., Harrison et al., 1992; Willett and Beaumont, 1994 and references therin). Several studies support the viability of the underthrusting and injection models for southern Tibet (Ding et al., 2022, and references therein), whereas thickening by distributed shortening (Houseman and England, 1993), or propagating northward (Tapponnier et al., 2001), may be acting in the north-eastern Tibet.

Our models show that the injection of the Indian crust along the Asian Moho is a viable mechanism that occurs at high convergence velocity and show a mechanism for subsequent exhumation. In our models ~550 km of incoming crust can be accommodated beneath the upper plate's crust, in the early stages, between ~8 and ~20 Myr from the start of the slowing convergence models. This mechanism operates as postulated by Zhao and Morgan (1987) and Beaumont et al. (2001), and is here reconciled with subduction dynamics. The switch from injection to exhumation in our models is due to the balance between injection pressure, due to the basal shear, and the load of the thickening plateau, then acting as a buttress, forcing the return flow to the front (e.g., Warren et al., 2008). Other works have suggested that exhumation may be driven by changes in relative plate motions. In these works, exhumation may be favoured by relative trench motions away from the upper plate (Piccolo et al., 2017; Sizova et al., 2012). However, this constrain is relaxed if the decreasing convergence is considered, showing orogeny late-stage extension although the trench is constantly advancing in our model. Other models invoke the onset of localised erosion along the Himalayan front, to drive the frontal crust exhumation (Beaumont et al., 2001). As said, this is likely driven by the pressure balance, while additional models (Figure s2) show that this process occurs even in the absence of erosion.

Here, the same crustal rheology is used across the margin to emphasise the role of convergence rate, controlling the crustal effective viscosity. Previous works, assuming constant convergence rate, have advocated for viscosity contrast to explain deep burial (e.g., Piccolo et al., 2017) and flow (e.g., Royden, 1997). Our results show that a range of end-members, from pure-shear thickening to exhumation, flow and underthrusting, may be explained by the rocks' shear rate-dependent weakening (e.g., Knight et al., 2021), therefore invoking pre-collisional viscosity contrasts may be unwarranted. Other works showed that the viscosity contrast between downgoing and upper plate's crust, may limit the expansion of the orogen towards the upper plate (Chen et al., 2017; Li et al., 2016). Indeed, this may critically depend on the varying properties of the wide Asian lithosphere (Kelly et al., 2019), which are not addressed here.

At depth, the delamination of part of the Asian lithosphere has been invoked to explain the Miocene volcanism and southern Plateau uplift. Published models propose the advance of the subducting Indian lithosphere driving thickening of the weaker Asian lithosphere beyond stability (Kelly et al., 2019; Li et al., 2016), and the replacement in the early stages by Indian rocks beneath Tibet (Liu et al., 2023). Our models show a range of similar mechanisms, from the complete underthrusting of Asia by Indian lithosphere forcing Lhasa Terrane's lithosphere delamination, during fast convergence, to no delamination in the slow models. However, in our models this occurs as a late-stage feature, in agreement with Kelly et al. (2019), and Li et al. (2016). In summary, our models reproduce these boundary conditions and suggest that the role of convergence rate deceleration fundamentally controls the evolution of the orogeny and that the role of the rheology difference between the Indian and Asian crust may be overstated.

5. CONCLUSIONS

A known feature of the Himalayan-Tibetan orogeny is the long-lasting decreasing rate of convergence, as the ocean closed, and continents collided. Here, a thermo-mechanical model is used to address the impact of decreasing convergence in the structuring of orogenies by comparing them to similar models with constant convergence velocity. The models show that the evolution of resulting from decreasing convergence velocity is remarkably different from an orogeny achieved at

constant rates. At high constant convergence rates, the subducting crust is buried and then injected as a channel along the Moho of the upper plate crust causing uplift of the overriding crust with little internal deformation. The buried and injected crust is then exhumed to the front of the orogeny. At low constant convergence rates, folding and faulting are the dominant structural styles, yet neither exhumation nor channel flow occurs. In contrast, for a decreasing convergence rate the structures formed early are similar to those of fast convergence but these are abandoned or overprinted, as convergence rate decreases. This is achieved during a transient phase that moves the system towards a new orogenic equilibrium. Slowing convergence decreases basal shearing and compression, allowing thermal re-equilibration and flow. This triggers a widening of the orogeny giving rise to a fold-and-thrust belt at the front of the orogeny, while leading to the “collapse” of the plateau, reflected by a decrease in topography. Decreasing convergence models reproduce the fast early growth of the Tibetan Plateau, its transient destabilisation and late-stage collapse, behind an expanding Himalayan fold-and-thrust belt.

Acknowledgements

The authors acknowledge and pay our respects to the Boonwurrung, Wurundjeri (Monash) and Nyungar (Curtin) peoples who are the Traditional Custodians of the Land this research was conducted on. We acknowledge support from Australian Research Council grants FT170100254 (awarded to F.A.C) FT220100566 (supporting B.S.K). L.D.Z was supported by the EU project “A Digital Twin for Geophysical Extremes” (DT-GEO) (No: 101058129) and the European Research Council (ERC) Synergy Grant “Fault Activation and Earthquake Rupture” (FEAR) (No: 856559). The authors acknowledge AuScope for their continued support in the development of the Underworld code. The authors acknowledge the provision of resources and services from the National Computational Infrastructure (NCI), which is supported by the Australian Government.

Data Availability

A setup file is available online (https://zenodo.org/doi/10.5281/zenodo.10036027), where the key parameters can be modified to replicate each model, using Underworld2 (https://zenodo.org/doi/10.5281/zenodo.1436039.

Declaration of Competing Interests

The authors declare that they have no known competing financial interests or personal relationships that could have appeared to influence the work reported in this manuscript.

References

Ader, T., Avouac, J.-P., Liu-Zeng, J., Lyon-Caen, H., Bollinger, L., Galetzka, J., Genrich, J., Thomas, M., Chanard, K., Sapkota, S.N., Rajaure, S., Shrestha, P., Ding, L., Flouzat, M., 2012. Convergence rate across the Nepal Himalaya and interseismic coupling on the Main Himalayan Thrust: Implications for seismic hazard: COUPLING ON THE MHT. J. Geophys. Res. Solid Earth 117, n/a-n/a. https://doi.org/10.1029/2011JB009071

Beaumont, C., Jamieson, R.A., Nguyen, M.H., Lee, B., 2001. Himalayan tectonics explained by extrusion of a low-viscosity crustal channel coupled to focused surface denudation. Nature 414, 738–742. https://doi.org/10.1038/414738a

Beucher, R., Moresi, L., Giordani, J., Mansour, J., Sandiford, D., Farrington, R., Mondy, L., Mallard, C., Rey, P., Duclaux, G., Kaluza, O., Laik, A., Morón, S., 2019. UWGeodynamics: A teaching and research tool for numerical geodynamic modelling. J. Open Source Softw. 4, 1136. https://doi.org/10.21105/joss.01136

Burchfiel, B.C., Zhiliang, C., Hodges, K.V., Yuping, L., Royden, L.H., Changrong, D., Jiene, X., 1992. The South Tibetan Detachment System, Himalayan Orogen: Extension Contemporaneous With and Parallel to Shortening in a Collisional Mountain Belt, in: Burchfiel, B.C., Zhiliang, C., Hodges, K.V., Yuping, L., Royden, L.H., Changrong, D., Xujiene (Eds.), The South Tibetan Detachment System, Himalayan Orogen: Extension Contemporaneous With and Parallel to Shortening in a Collisional Mountain Belt. Geological Society of America, p. 0. https://doi.org/10.1130/SPE269-p1

Chen, L., Capitanio, F.A., Liu, L., Gerya, T.V., 2017. Crustal rheology controls on the Tibetan plateau formation during India-Asia convergence. Nat. Commun. 8, 15992. https://doi.org/10.1038/ncomms15992

Clark, M.K., Royden, L.H., 2000. Topographic ooze: Building the eastern margin of Tibet by lower crustal flow 4.

de Sigoyer, J., Chavagnac, V., Blichert-Toft, J., Villa, I.M., Luais, B., Guillot, S., Cosca, M., Mascle, G., 2000. Dating the Indian continental subduction and collisional thickening in the northwest Himalaya: Multichronology of the Tso Morari eclogites. Geology 28, 487–490. https://doi.org/10.1130/0091-7613(2000)28<487:DTICSA>2.0.CO;2

DeCelles, P.G., Robinson, D.M., Quade, J., Ojha, T.P., Garzione, C.N., Copeland, P., Upreti, B.N., 2001. Stratigraphy, structure, and tectonic evolution of the Himalayan fold-thrust belt in western Nepal. Tectonics 20, 487–509. https://doi.org/10.1029/2000TC001226

DeCelles, P.G., Robinson, D.M., Zandt, G., 2002. Implications of shortening in the Himalayan fold-thrust belt for uplift of the Tibetan Plateau. Tectonics 21, 12-1-12–25. https://doi.org/10.1029/2001TC001322

Ding, L., Kapp, P., Cai, F., Garzione, C.N., Xiong, Z., Wang, H., Wang, C., 2022. Timing and mechanisms of Tibetan Plateau uplift. Nat. Rev. Earth Environ. 3, 652–667. https://doi.org/10.1038/s43017-022-00318-4

England, P., Molnar, P., 2005. Late Quaternary to decadal velocity fields in Asia. J. Geophys. Res. Solid Earth 110. https://doi.org/10.1029/2004JB003541

Faccenda, M., Minelli, G., Gerya, T.V., 2009. Coupled and decoupled regimes of continental collision: Numerical modeling. Earth Planet. Sci. Lett. 278, 337–349. https://doi.org/10.1016/j.epsl.2008.12.021

655 Finch, M., Hasalová, P., Weinberg, R.F., Fanning, C.M., 2014. Switch from thrusting
656 to normal shearing in the Zanskar shear zone, NW Himalaya: Implications for
657 channel flow. GSA Bull. 126, 892–924. https://doi.org/10.1130/B30817.1
658 Gao, R., Lu, Z.W., Klemperer, S.L., Wang, H.Y., Dong, S.W., Li, W.H., Li, H.Q.,
659 2016. Crustal-scale duplexing beneath the Yarlung Zangbo suture in the
660 western Himalaya. Nat. Geosci. 9, 555-+. https://doi.org/10.1038/ngeo2730
661 Gerya, T.V., Perchuk, L.L., Burg, J.-P., 2008. Transient hot channels: Perpetrating
662 and regurgitating ultrahigh-pressure, high-temperature crust–mantle
663 associations in collision belts. Lithos, Rocks Generated under Extreme
664 Pressure and Temperature Conditions: Mechanisms, Concepts, Models 103,
665 236–256. https://doi.org/10.1016/j.lithos.2007.09.017
666 Gibbons, A.D., Zahirovic, S., Müller, R.D., Whittaker, J.M., Yatheesh, V., 2015. A
667 tectonic model reconciling evidence for the collisions between India, Eurasia
668 and intra-oceanic arcs of the central-eastern Tethys. Gondwana Res. 28,
669 451–492. https://doi.org/10.1016/j.gr.2015.01.001
670 Godin, L., Grujic, D., Law, R.D., Searle, M.P., 2006. Channel flow, ductile extrusion
671 and exhumation in continental collision zones: an introduction. Geol. Soc.
672 Lond. Spec. Publ. 268, 1–23. https://doi.org/10.1144/GSL.SP.2006.268.01.01
673 Goscombe, B., Gray, D., Foster, D.A., 2018. Metamorphic response to collision in
674 the Central Himalayan Orogen. Gondwana Res. 57, 191–265.
675 https://doi.org/10.1016/j.gr.2018.02.002
676 Grujic, D., Casey, M., Davidson, C., Hollister, L.S., Kündig, R., Pavlis, T., Schmid, S.,
677 1996. Ductile extrusion of the Higher Himalayan Crystalline in Bhutan:
678 evidence from quartz microfabrics. Tectonophysics 260, 21–43.
679 https://doi.org/10.1016/0040-1951(96)00074-1
680 Grujic, D., Warren, C.J., Wooden, J.L., 2011. Rapid synconvergent exhumation of
681 Miocene-aged lower orogenic crust in the eastern Himalaya. Lithosphere 3,
682 346–366. https://doi.org/10.1130/L154.1
683 Guillot, S., Garzanti, E., Baratoux, D., Marquer, D., Mahéo, G., Sigoyer, J. de, 2003.
684 Reconstructing the total shortening history of the NW Himalaya. Geochem.
685 Geophys. Geosystems 4. https://doi.org/10.1029/2002GC000484
686 Harrison, T.M., Copeland, P., Kidd, W.S.F., Yin, A., 1992. Raising Tibet. Science
687 255, 1663–1670. https://doi.org/10.1126/science.255.5052.1663
688 Houseman, G., England, P., 1993. Crustal thickening versus lateral expulsion in the
689 Indian-Asian continental collision. J. Geophys. Res. Solid Earth 98, 12233–
690 12249. https://doi.org/10.1029/93JB00443
691 Hunter, N.J.R., Weinberg, R.F., Wilson, C.J.L., Luzin, V., Misra, S., 2018.
692 Microscopic anatomy of a “hot-on-cold” shear zone: Insights from quartzites of
693 the Main Central Thrust in the Alaknanda region (Garhwal Himalaya). GSA
694 Bull. 130, 1519–1539. https://doi.org/10.1130/B31797.1
695 Ingalls, M., Rowley, D.B., Currie, B., Colman, A.S., 2016. Large-scale subduction of
696 continental crust implied by India–Asia mass-balance calculation. Nat. Geosci.
697 9, 848–853. https://doi.org/10.1038/ngeo2806
698 Jagoutz, O., Müntener, O., Schmidt, M.W., Burg, J.-P., 2011. The roles of flux- and
699 decompression melting and their respective fractionation lines for continental
700 crust formation: Evidence from the Kohistan arc. Earth Planet. Sci. Lett. 303,
701 25–36. https://doi.org/10.1016/j.epsl.2010.12.017
702 Jessup, M.J., Langille, J.M., Diedesch, T.F., Cottle, J.M., 2019. Gneiss Dome
703 Formation in the Himalaya and southern Tibet. Geol. Soc. Lond. Spec. Publ.
704 483, 401–422. https://doi.org/10.1144/SP483.15

Jessup, M.J., Law, R.D., Searle, M.P., Hubbard, M.S., 2006. Structural evolution and vorticity of flow during extrusion and exhumation of the Greater Himalayan Slab, Mount Everest Massif, Tibet/Nepal: implications for orogen-scale flow partitioning, in: Law, R.D., Searle, M.P., Godin, L. (Eds.), Channel Flow, Ductile Extrusion and Exhumation in Continental Collision Zones. Geological Society of London, p. 0. https://doi.org/10.1144/GSL.SP.2006.268.01.18

Kelly, S., Beaumont, C., Butler, J.P., 2019. Inherited terrane properties explain enigmatic post-collisional Himalayan-Tibetan evolution. Geology. https://doi.org/10.1130/G46701.1

Knight, B.S., Capitanio, F.A., Weinberg, R.F., 2021. Convergence Velocity Controls on the Structural Evolution of Orogens. Tectonics 40, e2020TC006570. https://doi.org/10.1029/2020TC006570

Kohn, M.J., 2014. Himalayan Metamorphism and Its Tectonic Implications. Annu. Rev. Earth Planet. Sci. 42, 381–419. https://doi.org/10.1146/annurev-earth-060313-055005

Kumar, P., Tewari, H.C., Sreenivas, B., 2019. Seismic Structure of the Central Indian Crust and its Implications on the Crustal Evolution. J. Geol. Soc. India 93, 163–170. https://doi.org/10.1007/s12594-019-1146-4

Lee, J., Hacker, B.R., Dinklage, W.S., Wang, Y., Gans, P., Calvert, A., Wan, J., Chen, W., Blythe, A.E., McClelland, W., 2000. Evolution of the Kangmar Dome, southern Tibet: Structural, petrologic, and thermochronologic constraints. Tectonics 19, 872–895. https://doi.org/10.1029/1999TC001147

Lee, T.-Y., Lawver, L.A., 1995. Cenozoic plate reconstruction of Southeast Asia. Tectonophysics, Southeast Asia Structure and Tectonics 251, 85–138. https://doi.org/10.1016/0040-1951(95)00023-2

Li, Z.-H., Liu, M., Gerya, T., 2016. Lithosphere delamination in continental collisional orogens: A systematic numerical study. J. Geophys. Res. Solid Earth 121, 5186–5211. https://doi.org/10.1002/2016JB013106

Liang, S., Gan, W., Shen, C., Xiao, G., Liu, J., Chen, W., Ding, X., Zhou, D., 2013. Three-dimensional velocity field of present-day crustal motion of the Tibetan Plateau derived from GPS measurements. J. Geophys. Res. Solid Earth 118, 5722–5732. https://doi.org/10.1002/2013JB010503

Liu, Liang, Liu, Lijun, Morgan, J.P., Xu, Y.-G., Chen, L., 2023. New constraints on Cenozoic subduction between India and Tibet. Nat. Commun. 14, 1963. https://doi.org/10.1038/s41467-023-37615-5

Lucazeau, F., 2019. Analysis and Mapping of an Updated Terrestrial Heat Flow Data Set. Geochem. Geophys. Geosystems 20, 4001–4024. https://doi.org/10.1029/2019GC008389

Maiti, G., Mandal, N., 2021. Early Miocene Exhumation of High-Pressure Rocks in the Himalaya: A Response to Reduced India-Asia Convergence Velocity. Front. Earth Sci. 9.

Mansour, J., Giordani, J., Moresi, L., Beucher, R., Kaluza, O., Velic, M., Farrington, R., Quenette, S., Beall, A., 2020. Underworld2: Python Geodynamics Modelling for Desktop, HPC and Cloud. J Open Source Softw 5, 1797. https://doi.org/10.21105/joss.01797

Mitsuishi, M., Wallis, S.R., Aoya, M., Lee, J., Wang, Y., 2012. E–W extension at 19Ma in the Kung Co area, S. Tibet: Evidence for contemporaneous E–W and N–S extension in the Himalayan orogen. Earth Planet. Sci. Lett. 325–326, 10–20. https://doi.org/10.1016/j.epsl.2011.11.013

754 Molnar, P., Stock, J.M., 2009. Slowing of India's convergence with Eurasia since 20
755 Ma and its implications for Tibetan mantle dynamics.
756 https://doi.org/10.1029/2008TC002271
757 Molnar, P., Tapponnier, P., 1975. Cenozoic Tectonics of Asia: Effects of a
758 Continental Collision. Science 189, 419–426.
759 Müller, R.D., Sdrolias, M., Gaina, C., Roest, W.R., 2008. Age, spreading rates, and
760 spreading asymmetry of the world's ocean crust. Geochem. Geophys.
761 Geosystems 9. https://doi.org/10.1029/2007GC001743
762 Nelson, K.D., Zhao, W., Brown, L.D., Kuo, J., Che, J., Liu, X., Klemperer, S.L.,
763 Makovsky, Y., Meissner, R., Mechie, J., Kind, R., Wenzel, F., Ni, J., Nabelek,
764 J., Leshou, C., Tan, H., Wei, W., Jones, A.G., Booker, J., Unsworth, M., Kidd,
765 W.S.F., Hauck, M., Alsdorf, D., Ross, A., Cogan, M., Wu, C., Sandvol, E.,
766 Edwards, M., 1996. Partially Molten Middle Crust Beneath Southern Tibet:
767 Synthesis of Project INDEPTH Results. Science 274, 1684–1688.
768 https://doi.org/10.1126/science.274.5293.1684
769 Piccolo, A., Faccenda, M., Carosi, R., Montomoli, C., Visonà, D., 2017. Crustal
770 strength control on structures and metamorphism in collisional orogens.
771 Tectonophysics. https://doi.org/10.1016/j.tecto.2017.09.018
772 Pichon, X.L., Fournier, M., Jolivet, L., 1992. Kinematics, topography, shortening, and
773 extrusion in the India-Eurasia collision. Tectonics 11, 1085–1098.
774 https://doi.org/10.1029/92TC01566
775 Replumaz, A., Kárason, H., van der Hilst, R.D., Besse, J., Tapponnier, P., 2004. 4-D
776 evolution of SE Asia's mantle from geological reconstructions and seismic
777 tomography. Earth Planet. Sci. Lett. 221, 103–115.
778 https://doi.org/10.1016/S0012-821X(04)00070-6
779 Replumaz, A., Negredo, A.M., Guillot, S., der Beek, P. van, Villaseñor, A., 2010.
780 Crustal mass budget and recycling during the India/Asia collision.
781 Tectonophysics 492, 99–107. https://doi.org/10.1016/j.tecto.2010.05.023
782 Robinson, N., Regetz, J., Guralnick, R.P., 2014. EarthEnv-DEM90: A nearly-global,
783 void-free, multi-scale smoothed, 90m digital elevation model from fused
784 ASTER and SRTM data. ISPRS J. Photogramm. Remote Sens. 87, 57–67.
785 https://doi.org/10.1016/j.isprsjprs.2013.11.002
786 Rowley, D.B., 1996. Age of initiation of collision between India and Asia: A review of
787 stratigraphic data. Earth Planet. Sci. Lett. 145, 1–13.
788 https://doi.org/10.1016/S0012-821X(96)00201-4
789 Royden, L.H., 1997. Surface Deformation and Lower Crustal Flow in Eastern Tibet.
790 Science 276, 788–790. https://doi.org/10.1126/science.276.5313.788
791 Searle, M.P., 2015. Mountain Building, Tectonic Evolution, Rheology, and Crustal
792 Flow in the Himalaya, Karakoram, and Tibet, in: Treatise on Geophysics.
793 Elsevier. Elsevier, pp. 469–511. https://doi.org/10.1016/B978-0-444-53802-
794 4.00121-4
795 Searle, M.P., Hacker, B.R., 2019. Structural and metamorphic evolution of the
796 Karakoram and Pamir following India–Kohistan–Asia collision. Geol. Soc.
797 Lond. Spec. Publ. 483, 555–582. https://doi.org/10.1144/SP483.6
798 Sizova, E., Gerya, T., Brown, M., 2012. Exhumation mechanisms of melt-bearing
799 ultrahigh pressure crustal rocks during collision of spontaneously moving
800 plates. J. Metamorph. Geol. 30, 927–955. https://doi.org/10.1111/j.1525-
801 1314.2012.01004.x
802 Spain, M., Hirn, A., 1997. Seismic structure and evidence for eclogitization during the
803 Himalayan convergence. Tectonophys. Collisional Orogens Zones Act.

Transf. Crust Mantle, Collisional Orogens: Zones of Active Transfer Between Crust and Mantle 273, 1–16. https://doi.org/10.1016/S0040-1951(96)00285-5

Streule, M.J., Strachan, R.A., Searle, M.P., Law, R.D., 2010. Comparing Tibet-Himalayan and Caledonian crustal architecture, evolution and mountain building processes. Geol Soc Lond Spec Publ 335, 207–232. https://doi.org/10.1144/SP335.10

Tapponnier, P., Zhiqin, X., Roger, F., Meyer, B., Arnaud, N., Wittlinger, G., Jingsui, Y., 2001. Oblique Stepwise Rise and Growth of the Tibet Plateau. Science 294, 1671–1677. https://doi.org/10.1126/science.105978

Unsworth, M.J., Jones, A.G., Wei, W., Marquis, G., Gokarn, S.G., Spratt, J.E., Bedrosian, P., Booker, J., Leshou, C., Clarke, G., Shenghui, L., Chanhong, L., Ming, D., Sheng, J., Solon, K., Handong, T., Ledo, J., Roberts, B., The INDEPTH-MT team, 2005. Crustal rheology of the Himalaya and Southern Tibet inferred from magnetotelluric data. Nature 438, 78–81. https://doi.org/10.1038/nature04154

van Hinsbergen, D.J.J., Kapp, P., Dupont-Nivet, G., Lippert, P.C., DeCelles, P.G., Torsvik, T.H., 2011. Restoration of Cenozoic deformation in Asia and the size of Greater India. Tectonics 30. https://doi.org/10.1029/2011TC002908

Vogt, K., Matenco, L., Cloetingh, S., 2017. Crustal mechanics control the geometry of mountain belts. Insights from numerical modelling. Earth Planet. Sci. Lett. 460, 12–21. https://doi.org/10.1016/j.epsl.2016.11.016

Wang, C., Dai, J., Zhao, X., Li, Y., Graham, S.A., He, D., Ran, B., Meng, J., 2014. Outward-growth of the Tibetan Plateau during the Cenozoic: A review. Tectonophysics 621, 1–43. https://doi.org/10.1016/j.tecto.2014.01.036

Wang, L., Barbot, S., 2023. Three-dimensional kinematics of the India–Eurasia collision. Commun. Earth Environ. 4, 164. https://doi.org/10.1038/s43247-023-00815-4

Warren, C.J., Beaumont, C., Jamieson, R.A., 2008. Deep subduction and rapid exhumation: Role of crustal strength and strain weakening in continental subduction and ultrahigh-pressure rock exhumation. Tectonics 27. https://doi.org/10.1029/2008TC002292

Willett, S.D., Beaumont, C., 1994. Subduction of Asian lithospheric mantle beneath Tibet inferred from models of continental collision. Nature 369, 642–645. https://doi.org/10.1038/369642a0

Yakovlev, P.V., Clark, M.K., 2014. Conservation and redistribution of crust during the Indo-Asian collision. Tectonics 33, 1016–1027. https://doi.org/10.1002/2013TC003469

Yin, A., Harrison, T.M., 2000. Geologic Evolution of the Himalayan-Tibetan Orogen. Annu. Rev. Earth Planet. Sci. 28, 211–280. https://doi.org/10.1146/annurev.earth.28.1.211

Zhao, Q., Chen, Q., van Dam, T., She, Y., Wu, W., 2023. The vertical velocity field of the Tibetan Plateau and its surrounding areas derived from GPS and surface mass loading models. Earth Planet. Sci. Lett. 609, 118107. https://doi.org/10.1016/j.epsl.2023.118107

Zhao, W., Nelson, K.D., Che, J., Quo, J., Lu, D., Wu, C., Liu, X., 1993. Deep seismic reflection evidence for continental underthrusting beneath southern Tibet. Nature 366, 557–559. https://doi.org/10.1038/366557a0

Zhao, W.-L., Morgan, W.J., 1987. Injection of Indian crust into Tibetan lower crust: A two-dimensional finite element model study. Tectonics 6, 489–504. https://doi.org/10.1029/TC006i004p00489

854
855

Supplementary Material

1. Appendix A: Model setup

a. Geodynamic model

The 2D model is designed to simulate continental collision (Figure 2a). The model has a length (x) of 1792 km and a height (y) of 224 km. The grid is uniformly spaced at 1024 x 128 nodes, producing a grid resolution of 1.75 km, with 20 particles per cell to track material properties. Timesteps are determined by using (half of) the Courant–Friedrichs–Lewy (CFL) condition. A cell width of 1.75 km results in timesteps of ~44,000 years for a convergence velocity of 2 cm yr^{-1} and ~8,750 years at a convergence velocity of 10 cm yr^{-1}. In the fast to slow models, the timestep duration increases as the convergence velocity decreases.

The viscous rheology of the crust varies, with a quartzite rheology used for crust A and B, while a diabase rheology is used for crust C (supplementary table 1). The friction coefficient is kept constant for the different crustal blocks (fc = 0.3, supplementary table 1). A 45° dipping weak zone within the mantle lithosphere (x = 650 km) is included within the lithosphere, representing a pre-existing suture (Vogt et al., 2017). The weak zone has a wet olivine rheology and low friction coefficient (0.1), whilst the surrounding lithospheric mantle (LM) has a dry olivine rheology and high friction coefficient (0.6), presented in supplementary table 1. The pre-existing weakness is included within the lithospheric mantle to introduce a rheological heterogeneity that facilitates lithospheric subduction and localises deformation in the crust above (Burg and Gerya, 2005; Knight et al., 2021; Vogt et al., 2017; Willingshofer et al., 2013).

A constant temperature (T = 0 °C) is applied to the top boundary, with no heat flux across the side walls. The initial internal temperature distribution follows a geothermal gradient of 25 °C km^{-1} for the first 10 km and then 12 °C km^{-1} until a temperature of 1300 °C is reached at the lithosphere-asthenosphere boundary (LAB) at a depth of 97.5 km. We neglect adiabatic gradients and keep the underlying mantle at 1300 ˚C. The temperature is unconstrained on the bottom boundary to allow the temperature to evolve freely as the lithosphere subducts.

The model uses a no-slip condition on the right (v_x, v_y = 0) boundary and a free-slip condition on the top (v_y = 0) boundary. The bottom boundary is

unconstrained, allowing for inflow and outflow of material, implying the model overlies an infinite half-space with an inviscid fluid (Gerya, 2009). The convergence velocity is applied on the left side wall across the crust and mantle lithosphere. Below the lithosphere (y < - 97.5 km), the velocity linearly decreases from the convergence velocity at base of the lithosphere to zero at the bottom of the left wall. Above the crust, an inflow/outflow boundary is set across the sticky air layer (y > 0 km) to allow topography to develop.

Supplementary table 1: Initial material properties used for the visco-plastic rheology. ρ_o is the density at the surface. A is the pre-exponential factor, n, is the stress exponent, E is the activation energy, f_c is the friction coefficient, C is the cohesion at the surface, α is the coefficient of thermal expansion and H_r is the internal heating rate.

Material	*Sediment*	*Crust A & B*	*Crust C*	*Mantle*		*Weak Zone*	
Rheology	Quartzite[a]	Quartzite[a]	Diabase[a]	Olivine[b]		Wet Olivine[b]	
Deformation mechanism	Dislocation	Dislocation	Dislocation	Dislocation	Diffusion	Dislocation	Diffusion
Strength factor (χ)	0.5	1	1	1	1	1	1
A ($MPa^{-n} s^{-1}$)	6.7×10^{-6}	6.7×10^{-6}	2.0×10^{-4}	1.1×10^{5}	1.5×10^{9}	1.6×10^{3}	2.5×10^{7}
n	2.4	2.4	3.4	3.5	1.0	3.5	1.0
E ($J\ mol^{-1}$)	1.56×10^{5}	1.56×10^{5}	2.60×10^{5}	5.30×10^{5}	3.75×10^{5}	5.20×10^{5}	3.75×10^{5}
V ($m^3\ mol^{-1}$)	0	0	0	6.0×10^{-6}	6.0×10^{-6}	2.3×10^{-5}	1.0×10^{-5}
C, C_w (MPa)	10, 1	10, 1	10, 1	10		10, 1	
f_c, $f_{c,w}$	0.2, 0.1	0.3, 0.15	0.3, 0.15	0.6		0.1, 0.05	

ρ_0 (kg m^{-3})	2,500	2,700	2,700	3,300	3,300
H_r (μW m^{-3})	2	2	2	0.02	0.02

[a](Ranalli, 1995) [b](Hirth and Kohlstedt, 2003).

b. Surface processes

Linear hillslope diffusion (D) is included in the model, which is the rate at which variations in topography diffuse over, to simulate erosion and sedimentation at the crust-air interface of the model. The evolution of the surface topography (h) is modelled assuming the short-range transport of material as a linear flux (q_s) which is proportional to the surface slope (Avouac, 1993; Culling, 1960):

$$q_s = -D\frac{dh}{dx}$$

where D is the surface diffusion constant, expressed as a unit area over unit time (m^2 yr^{-1}), that determines the amount of erosion and sedimentation taking place at the surface and $\frac{dh}{dx}$ is the vertical height difference between adjacent particles that track the surface (in unit length, m). As the surface of the model is represented as a line (1D), the change in surface height over time ($\frac{dh}{dt}$) is reduced to (Gerya, 2009):

$$\frac{dh}{dt} = \frac{dq_s}{dx}$$

2. Appendix B: Additional Figures

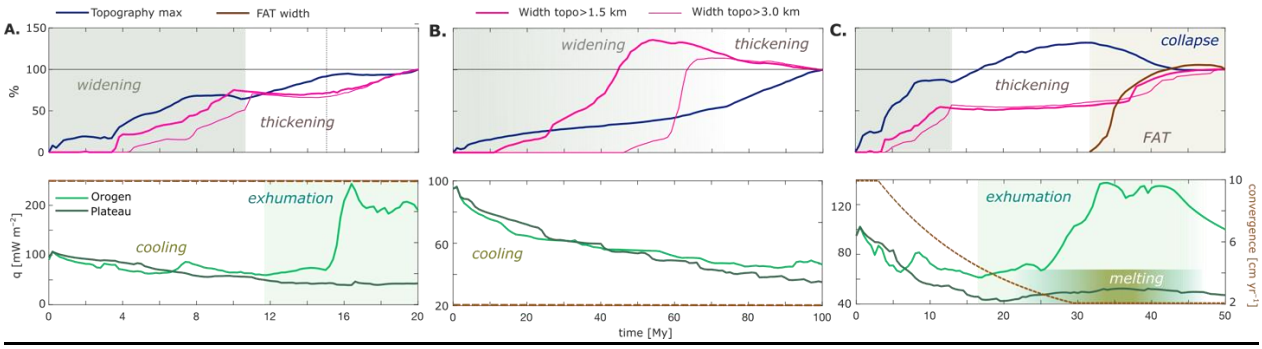

Figure S1: Evolution of the orogen width (top panels) and heat flow (bottom panels) of each model over time. A) Fast model (10 cm yr^{-1}), B) model (2 cm yr^{-1}) and C) fast to slow (decelerating) model (10 – 2 cm yr^{-1}). The fast (A) and fast to slow (C) models show a general cooling trend of the plateau due to crustal thickening and cooling of the crust in that region, whilst the at the front of the plateau undergoes a major heating event due to return flow at the front of the orogen. The slow model (B) shows a cooling trend in both the orogen and plateau throughout the evolution of the model due to slow thickening of the crust and thermal diffusion.

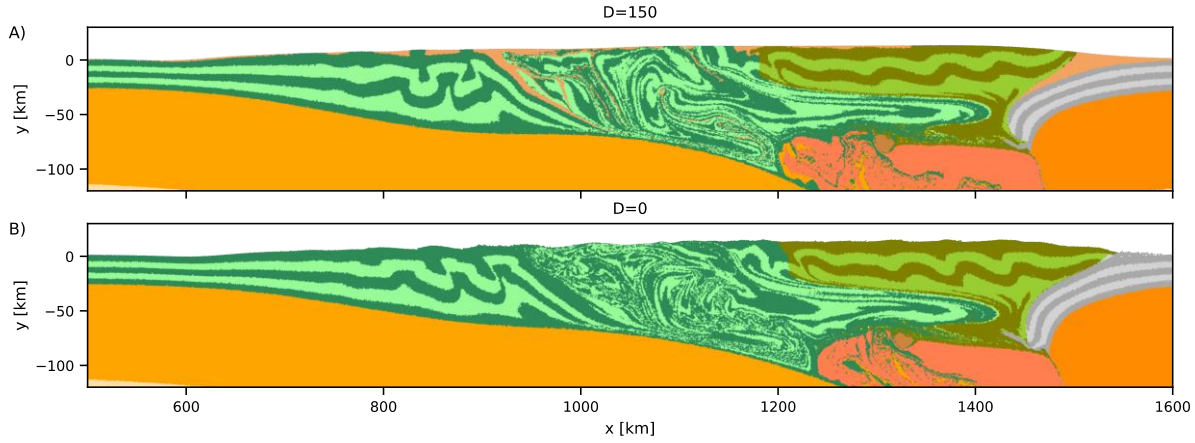

Figure S2: Comparison of the fast to slow model A) with (D = 150 m^2 yr^{-1} - DV10-2) and B) without (D = 0 m^2 yr^{-1} - DV10-2_D0) sedimentation and erosion after 2000 km of convergence over 50 Myr. All major structural features are present in both models, with some small variations due to the redistribution of material through sedimentation and erosion in (A).

1. Appendix C: Models run

2. *Supplementary table 2: List of all models tested. Model name, total time, velocity boundary condition, surface processes, internal heating rates (of the crust) and crustal density. The behaviour of the 3 end-member models (green) is consistent with all the model tested.*

Model name	Total model time [Myr]	Velocity condition [cm yr^{-1}]	Surface diffusivity (D) [m^2 yr^{-1}]	Internal heating rate (H_r) [μW m^{-3}]	Crustal density (ρ_0) [kg m^{-3}]

CV10	*20*	*Constant- 10*	*150*	*2*	*2700*
CV10_ρ2800	20	Constant- 10	150	2	2800
CV10_ρ2900	20	Constant- 10	150	2	2900
CV10_D0	20	Constant- 10	0	2	2700
CV10_D300	20	Constant- 10	300	2	2700
CV10_1H_r	20	Constant- 10	150	1	2700
CV2	*100*	*Constant- 10*	*150*	*2*	*2700*
CV2_ρ2800	100	Constant- 10	150	2	2800
CV2_ρ2900	100	Constant- 10	150	2	2900
CV2_D0	100	Constant- 10	0	2	2700
CV2_D300	100	Constant- 10	300	2	2700
CV2_1H_r	100	Constant- 10	150	1	2700
DV10-2	*50*	*Decreasing- 10 to 2*	*150*	*2*	*2700*
DV10-2_ρ2800	50	Decreasing- 10 to 2	150	2	2800
DV10-2_ρ2900	50	Decreasing- 10 to 2	150	2	2900
DV10-2_D0	50	Decreasing- 10 to 2	0	2	2700
DV10-2_D300	50	Decreasing- 10 to 2	300	2	2700
DV10-2_1H_r	50	Decreasing- 10 to 2	150	1	2700

930

931

References

Avouac, J.-P., 1993. Analysis of scarp profiles: Evaluation of errors in morphologic dating. J. Geophys. Res. Solid Earth 98, 6745–6754. https://doi.org/10.1029/92JB01962

Burg, J.-P., Gerya, T.V., 2005. The role of viscous heating in Barrovian metamorphism of collisional orogens: thermomechanical models and application to the Lepontine Dome in the Central Alps. J. Metamorph. Geol. 23, 75–95. https://doi.org/10.1111/j.1525-1314.2005.00563.x

Culling, W.E.H., 1960. Analytical Theory of Erosion. J. Geol. 68, 336–344.

Gerya, T., 2009. Introduction to Numerical Geodynamic Modelling. Cambridge University Press, Cambridge. https://doi.org/10.1017/CBO9780511809101

Hirth, G., Kohlstedt, D., 2003. Rheology of the upper mantle and the mantle wedge: A view from the experimentalists, in: Eiler, J. (Ed.), Geophysical Monograph Series. American Geophysical Union, Washington, D. C., pp. 83–105. https://doi.org/10.1029/138GM06

Knight, B.S., Capitanio, F.A., Weinberg, R.F., 2021. Convergence Velocity Controls on the Structural Evolution of Orogens. Tectonics 40, e2020TC006570. https://doi.org/10.1029/2020TC006570

Ranalli, G., 1995. Rheology of the Earth. Springer Science & Business Media.

Vogt, K., Matenco, L., Cloetingh, S., 2017. Crustal mechanics control the geometry of mountain belts. Insights from numerical modelling. Earth Planet. Sci. Lett. 460, 12–21. https://doi.org/10.1016/j.epsl.2016.11.016

Willingshofer, E., Sokoutis, D., Luth, S.W., Beekman, F., Cloetingh, S., 2013. Subduction and deformation of the continental lithosphere in response to plate and crust-mantle coupling. Geology 41, 1239–1242. https://doi.org/10.1130/G34815.1